Biophysical Journal, Volume *115*

Supplemental Information

Balance between Force Generation and Relaxation Leads to Pulsed Contraction of Actomyosin Networks

Qilin Yu, Jing Li, Michael P. Murrell, and Taeyoon Kim

SUPPLEMENTAL INFORMATION

Brownian dynamics via the Langevin equation

In our agent-based model, F-actins consist of serially connected cylindrical segments with polarity: barbed and pointed ends. Actin cross-linking proteins (ACPs) are comprised of a pair of cylindrical segments. Each motor is modeled to mimic geometry of myosin thick filaments; each motor has a backbone structure with four arms ($N_a = 4$), and each of the arms represents 8 myosin heads ($N_h = 8$). Thus, the total number of myosin heads represented by one motor is 32, which is not very different from 56 myosin heads in one non-muscle myosin thick filament (1). Displacements of the segments are determined by the Langevin equation with negligence of inertia:

$$\mathbf{F}_i - \zeta_i \frac{\mathrm{d}\mathbf{r}_i}{\mathrm{d}t} + \mathbf{F}_i^{\mathrm{T}} = 0 \tag{S1}$$

where $\mathbf{r}_i$ is a position vector of the ith element, ζ_i is a drag coefficient, t is time, $\mathbf{F}_i$ is deterministic force, and $\mathbf{F}_i^{\mathrm{T}}$ is a stochastic force satisfying the fluctuation-dissipation theorem (2):

$$\left\langle \mathbf{F}_i^{\mathrm{T}}(t)\mathbf{F}_j^{\mathrm{T}}(t) \right\rangle = \frac{2k_{\mathrm{B}}T\zeta_i\delta_{ij}}{\Delta t}\boldsymbol{\delta} \tag{S2}$$

where $\boldsymbol{\delta}$ is a second-order tensor, δ_{ij} is the Kronecker delta, and $\Delta t = 1.15 \times 10^{-5}$ s is a time step. Drag coefficients are computed using an approximated form for a cylindrical object (3):

$$\zeta_i = 3\pi\mu r_{\mathrm{c},i}\frac{3 + 2r_{0,i}/r_{\mathrm{c},i}}{5} \tag{S3}$$

where μ is viscosity of surrounding medium, and $r_{0,i}$ and $r_{\mathrm{c},i}$ are length and diameter of a segment, respectively. Positions of all the cylindrical segments are updated every time step using the Euler integration scheme:

$$\mathbf{r}_i(t + \Delta t) = \mathbf{r}_i(t) + \frac{\mathrm{d}\mathbf{r}_i}{\mathrm{d}t}\Delta t = \mathbf{r}_i(t) + \frac{1}{\zeta_i}\left(\mathbf{F}_i + \mathbf{F}_i^{\mathrm{T}}\right)\Delta t \tag{S4}$$

Deterministic forces

Deterministic forces include extensional forces maintaining equilibrium lengths, bending forces maintaining equilibrium angles, and repulsive forces accounting for volume-exclusion effects between actin segments. The extensional and bending forces originate from the following potentials:

$$U_{\mathrm{s}} = \frac{1}{2}\kappa_{\mathrm{s}}(r - r_0)^2 \tag{S5}$$

$$U_{\mathrm{b}} = \frac{1}{2}\kappa_{\mathrm{b}}\left(\theta - \theta_0\right)^2 \tag{S6}$$

where κ_{s} and κ_{b} are extensional and bending stiffnesses, r and r_0 is instantaneous and equilibrium lengths of cylindrical segments, and θ and θ_0 are instantaneous and equilibrium angles formed by adjacent segments. An equilibrium length of actin segments ($r_{0,\mathrm{A}}$ = 140 nm) and an equilibrium angle formed by two adjacent actin segments ($\theta_{0,\mathrm{A}}$ = 0 rad) are maintained by extensional ($\kappa_{\mathrm{s,A}}$) and bending stiffnesses of actins ($\kappa_{\mathrm{b,A}}$), respectively. The reference value of $\kappa_{\mathrm{b,A}}$ corresponds to the persistence length of 9 μm (4). An equilibrium length of ACP arms ($r_{0,\mathrm{ACP}}$ = 23.5 nm) and an equilibrium angle formed by two arms of each ACP ($\theta_{0,\mathrm{ACP}}$ = 0 rad) are regulated by extensional ($\kappa_{\mathrm{s,ACP}}$) and bending stiffnesses of ACPs ($\kappa_{\mathrm{b,ACP}}$), respectively. An equilibrium length of motor backbone segments ($r_{\mathrm{s,M1}}$= 42 nm) and an equilibrium angle formed by adjacent backbone segments ($\theta_{0,\mathrm{M}}$ = 0 rad) are maintained by extensional ($\kappa_{\mathrm{s,M1}}$) and bending stiffnesses ($\kappa_{\mathrm{b,M}}$), respectively. The value of $\kappa_{\mathrm{s,M1}}$ is equal to that of $\kappa_{\mathrm{s,A}}$, whereas the value of $\kappa_{\mathrm{b,M}}$ is larger than that of $\kappa_{\mathrm{b,A}}$. Extension of each motor arm is regulated by the two-spring model with stiffnesses of transverse ($\kappa_{\mathrm{s,M2}}$) and longitudinal springs ($\kappa_{\mathrm{s,M3}}$). The transverse spring maintains an equilibrium distance ($r_{0,\mathrm{M2}}$ = 13.5 nm) between an endpoint of a motor backbone and actin segment where the arm of the motor binds, whereas the longitudinal spring helps maintain a right angle between the motor arm and the actin segment ($r_{0,\mathrm{M3}}$ = 0 nm).

Repulsive force is represented by a harmonic potential (5):

$$U_{\mathrm{r}} = \begin{cases} \dfrac{1}{2}\kappa_{\mathrm{r}}\left(r_{12} - r_{\mathrm{c,A}}\right)^2 & \text{if} \quad r_{12} < r_{\mathrm{c,A}} \\ 0 & \text{if} \quad r_{12} \geq r_{\mathrm{c,A}} \end{cases} \tag{S7}$$

where κ_r is strength of repulsive force, and r_{12} is the minimum distance between two actin segments. Forces exerted on actin segments by bound ACPs and motors or by the repulsive force are distributed onto the barbed and pointed ends of the actin segments as described in our previous work (6).

Dynamics of ACPs

ACPs bind to binding sites located on actin segments every 7 nm with no preference of contact angle at a constant rate. ACPs also unbind from F-actin in a force-dependent manner following Bell's equation (7):

$$k_{u,ACP} = \begin{cases} k^0_{u,ACP} \exp\left(\dfrac{x_{u,ACP} \left| \vec{F}_{s,ACP} \right|}{k_B T} \right) & \text{if } r \geq r_{0,ACP} \\ k^0_{u,ACP} & \text{if } r < r_{0,ACP} \end{cases} \quad \text{(S8)}$$

where $\left| \vec{F}_{s,ACP} \right|$ is spring force exerted on an ACP arm, $k^0_{u,ACP}$ is the zero-force unbinding rate constant, $x_{u,ACP}$ is sensitivity to applied force, and $k_B T$ is thermal energy. Values of $k^0_{u,ACP}$ (= 0.115 s^{-1}) and $x_{u,ACP}$ (= 1.04×10^{-10} m) are determined based on filamin A (8).

Dynamics of motors

Motor arms bind to binding sites on actin segments at a rate of $40N_h$ s^{-1}, where N_h = 8 is the number of myosin heads represented by each motor arm. Walking ($k_{w,M}$) and unbinding rates ($k_{u,M}$) of the motor arms are determined by the parallel cluster model to mimic the mechanochemical cycle of non-muscle myosin II (9, 10). Details of implementation and benchmarking of the parallel cluster model in our models are extensively described in our previous study (11). Note that $k_{w,M}$ and $k_{u,M}$ are lower with higher applied load since motors exhibit a catch-bond behavior. Unloaded walking velocity and stall force of motors are set to ~140 nm/s and ~5.7 pN, respectively.

Justification and limitation of an empirical equation for F-actin severing

Eq. 1 describes the relationship between the severing rate ($k_{s,A}$) and the sum of bending angles at two ends of each actin segment ($\theta_{s,A}$). We determined this relationship in an empirical fashion as shown in our previous study (12). An intro experiment showed that F-actin severing occurs only at relatively large bending angles ($57 \pm 9^\circ$) during thermal fluctuation (13). To mimic the experiment, we ran a simulation only with F-actins and measured bending angles of thermally fluctuating F-actins. We found that the probability of occurrence of a bending angle exponentially decreases as the angle is greater. This implies that $k_{s,A}$ needs to be extremely sensitive to an increase in the bending angle in order to let severing events occur only at large bending angles. Thus, we assumed that $k_{s,A}$ exponentially increases as the bending angle increases (Eq. 1). As a result, values of $k_{s,A}^0$ used in this study may seem unrealistically small at a glance, but such small values are necessary. The reference value of λ_{sev} = 1.6 deg was determined by comparing the distribution of bending angles where severing occurred in the simulations with the experimental observation (13). A variation in $k_{s,A}^0$ does not affect the distribution of severing angles, but as $k_{s,A}^0$ is greater, severing events occur more frequently at all bending angles.

Although we devised the relationship by comparing with experimental results, we admit that this relationship may not reflect severing dynamics very rigorously and have some limitations. For determination of $k_{s,A}$, we used bending angles rather than the radius of curvature. In the in vitro experiments, it was observed that F-actin can often be bent in a non-uniform manner with a kink, and severing is more likely to occur near the kink (13, 14). Thus, they showed a relationship between the severing rate and a bending angle rather than the radius of

curvature. This indicates that the angle-dependent severing rate could be a better way to describe the F-actin severing induced by non-uniform bending. Since we used bending angles for determining $k_{s,A}$, it is possible that parameter values inducing pulsed contraction may vary depending on how F-actin is discretized into serially-connected cylindrical segments. However, when we reduced the length of actin cylindrical segments from 140 nm to 70 nm, pulsed contraction still took place with similar parameter values (Figs. 9a, b). This implies that F-actins in our simulations undergo non-uniform deformation induced by motor activities. (i.e. more bending on a certain part of F-actin than other parts) Since F-actin severing is simulated by disappearance of one actin segment, we used the sum of two bending angles because an increase in either of the angles would lead to the severing event on the segment.

We also tried to let the F-actin severing occur deterministically; severing immediately occurs at a bending angle greater than a critical angle, whereas severing never occurs below the critical angle. We observed that distinct pulsed contraction still emerged with such a deterministic relationship (Figs. S9c, d). This implies that emergence of pulsed contraction due to balance between force generation and global/local force relaxation is not sensitive to the choice of a specific model for F-actin severing. As long as F-actin severing occurs selectively at large angles, the pulsed contraction can be reproduced. Note that we do not try to find universal parameter values for pulsed contraction that work with any assumption. Our aim in this study is to provide insights into a possible mechanical mechanism for pulsed contraction observed in cells by showing that F-actin severing induced by buckling can drive the pulsed contraction via local force relaxation. Predictions from our computational study are rather qualitative, not very quantitative, due to uncertainty and limitations of the F-actin severing although our model reflects the treadmilling and severing of F-actins more accurately than previous models.

Determination of threshold values for quantification of the clustering behaviors

As explained in the main text, we used a threshold value for detection of clusters. Depending on the threshold value, results of the analysis can vary substantially. If the value is very low, the analysis method will detect too many trivial structures that are too small to be considered clusters. By contrast, if the value is too high, only very large clusters will be detected. Thus, the threshold value should be chosen carefully. To find an optimal value, we analyzed clustering behaviors in several cases. As examples, we show fluctuation of the actin density in all grids for 200 s under three conditions: (i) a network with a high treadmilling rate (120 s^{-1}), (ii) a network without motors, and (iii) a network with an intermediate treadmilling rate. The first and second cases show negligible contraction due to either very high force relaxation or very low force generation. All grids in the first and second cases exhibit only small fluctuation with a few small peaks (Figs. S8d, e, g, h). Peak actin density in each grid has an average value between 11 to 12 (Figs. S8a, b). All the peaks last for less than 20 s, so these peaks cannot represent significant clustering behaviors. However, the third case, with higher average density (Fig. S8c), shows distinct peaks whose density and duration are much larger than small fluctuation (Figs. S8f, i), and nascent pulsed clusters are clearly observed in network morphology. To capture the nascent pulsed clusters but ignore small peaks, we set the threshold value for density to be 12. Additionally, we set a threshold value for duration to be 20 s. The combination of the spatial and temporal threshold values enables us to detect most of the statistically significant clusters in a network. In a homogenous network, such combination prevents background fluctuations from being detected as nascent pulsed clusters (Fig. S8j).

Table S1. List of parameters employed in the model. For some of the parameters, references are provided if the parameters were determined based on specific previous studies.

Symbol	Definition	Value
$r_{0,A}$	Length of an actin segment	1.4×10^{-7} or 0.7×10^{-7} [m]
$r_{c,A}$	Diameter of an actin segment	7.0×10^{-9} [m] (15)
$\theta_{0,A}$	Bending angle formed by adjacent actin segments	0 [rad]
$\kappa_{s,A}$	Extensional stiffness of F-actin	1.69×10^{-2} [N/m]
$\kappa_{b,A}$	Bending stiffness of F-actin	2.64×10^{-19} [N·m] (4)
$r_{0,ACP}$	Length of an ACP arm	2.35×10^{-8} [m] (16)
$r_{c,ACP}$	Diameter of an ACP arm	1.0×10^{-8} [m]
$\theta_{0,ACP}$	Bending angle formed by two ACP arms	0 [rad]
$\kappa_{s,ACP}$	Extensional stiffness of ACP	2.0×10^{-3} [N/m]
$\kappa_{b,ACP}$	Bending stiffness of ACP	1.04×10^{-19} [N·m]
$r_{0,M1}$	Length of a motor backbone segment	4.2×10^{-8} [m]
$r_{0,M2}$	Length of a motor arm	1.35×10^{-8} [m]
$r_{c,M}$	Diameter of a motor arm	1.0×10^{-8} [m]
$\theta_{0,M}$	Bending angle formed by motor backbone segments	0 [rad]
$\kappa_{s,M1}$	Extensional stiffness of a motor backbone	1.69×10^{-2} [N/m]
$\kappa_{s,M2}$	Extensional stiffness 1 of a motor arm	1.0×10^{-3} [N/m]
$\kappa_{s,M3}$	Extensional stiffness 2 of a motor arm	1.0×10^{-3} [N/m]
$\kappa_{b,M}$	Bending stiffness of a motor backbone	5.07×10^{-18} [N·m]
N_h	Number of heads represented by a motor arm	8
N_a	Number of arms per motor	4
$k_{n,A}$	Nucleation rate of actin	0.0225 – 0.36 [$\mu M^{-1}s^{-1}$]
$k_{+,A}$	Polymerization rate of actin at the barbed end	15 - 240 [$\mu M^{-1}s^{-1}$]
$k_{-,A}$	Depolymerization rate of actin at the pointed end	15 - 240 [s^{-1}]
$k_{s,A}^0$	Zero-angle severing rate constant	10^{-60} – 10^{-10} [s^{-1}]
$\lambda_{s,A}$	Insensitivity of a severing rate to a bending angle	0.3 – 2.9 [deg]
$k_{u,ACP}^0$	Zero-force unbinding rate constant of ACP	0.115 [s^{-1}] (8)
$x_{u,ACP}$	Sensitivity of ACP unbinding to applied force	1.04×10^{-10} [m] (8)
κ_r	Strength of repulsive force	1.69×10^{-3} [N/m]
Δt	Time step	1.15×10^{-5} [s]
μ	Viscosity of surrounding medium	8.6×10^{-1} [kg/m·s]
k_BT	Thermal energy	4.142×10^{-21} [J]
C_A	Actin concentration	60 [μM]
R_M	Ratio of motor concentration to C_A	0.04
R_{ACP}	Ratio of ACP concentration to C_A	0.0025-0.16
$<L_f>$	Average length of F-actins	0.7 – 5.0 [μm]

SUPPLEMENTAL FIGURES

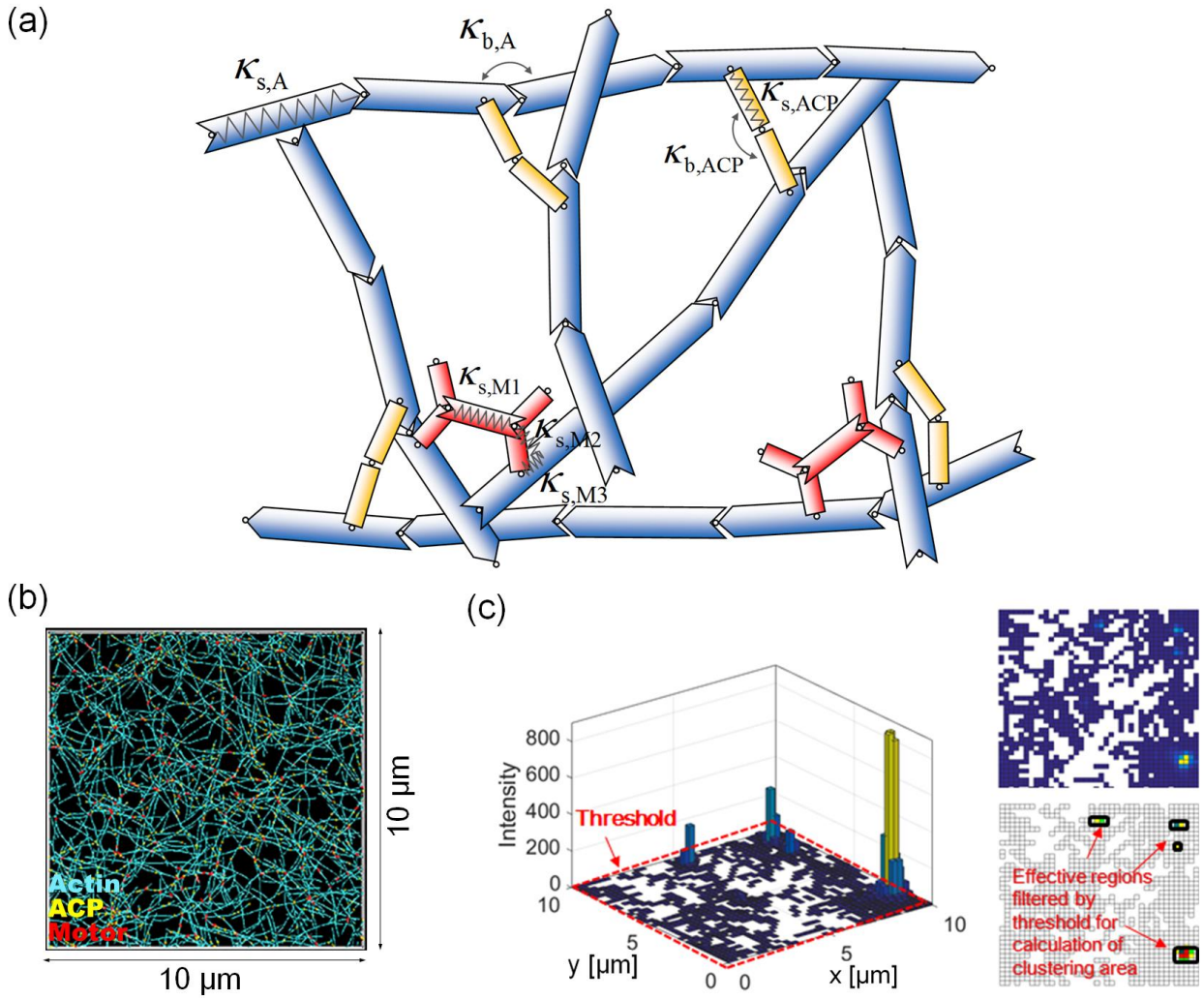

Figure S1. Model and analysis used in the study. (a) A schematic diagram showing an actomyosin network consisting of F-actin (cyan), actin crosslinking protein (yellow), and motor (red). These three elements are simplified by cylindrical segments. Equilibrium lengths of segments and equilibrium angles formed by adjacent segments are maintained by extensional stiffness (κ_s) and bending stiffness (κ_b), respectively. (b) An example of a network in a thin computational domain ($10 \times 10 \times 0.1$ μm). (c) Quantification of clusters based on actin density. A 3D histogram at each time point is created using density of actin segments. Then, adjacent regions whose actin density is above a certain threshold are considered one cluster. This analysis is repeated for all time points, and then clusters at two consecutive time points are correlated using criteria explained in the text.

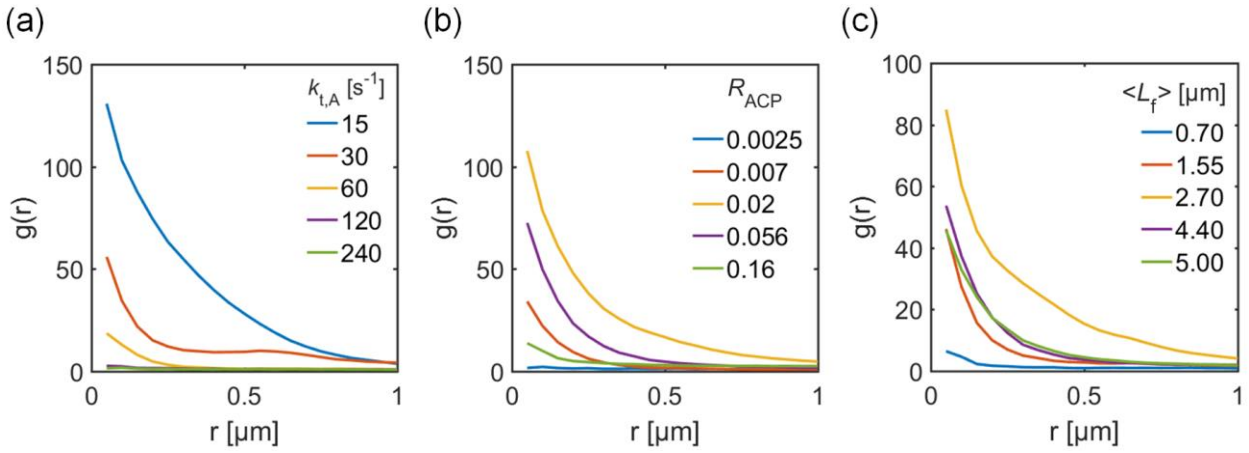

Figure S2. Radial distribution function as an additional measure for network heterogeneity. (a) Cases with various treadmilling rates shown in Fig. 1. (b) Cases with five different ACP density shown in Fig. 2. (c) Cases with five average F-actin lengths shown in Fig. 3. Higher values of $g(r)$ at smaller r indicate more heterogeneous network morphology.

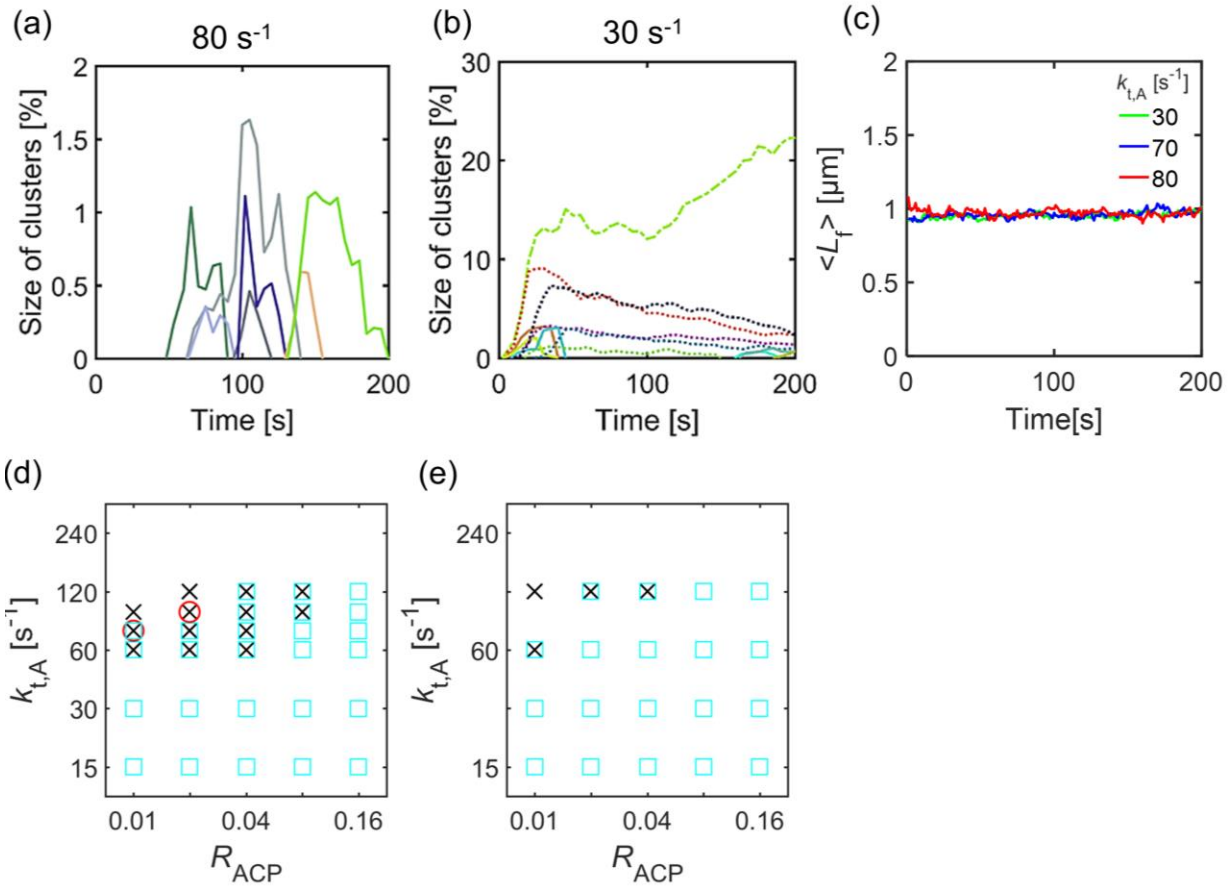

Figure S3. Examples of simulations showing small pulsed, fluctuating, decaying, and growing clusters. $k_{t,A}$ is set to be 30, 70 or 80 s^{-1} at R_M = 0.04, R_{ACP} = 0.01, and $<L_f>$ = 1 μm. (a, b) Time evolution of percentage of actin segments located within all identified clusters with two different $k_{t,A}$. Random colors are assigned to curves to distinguish each cluster. Pulsed, decaying, and irreversible (fluctuating and growing) clusters are shown by solid, dotted, and dot-dashed lines, respectively. In (a), only small pulsed clusters appear. In (b), decaying and growing clusters are formed. Some small clusters still form but disassemble very rapidly at early times. (c) Time evolution of average length of F-actins ($<L_f>$) for two cases shown in (a-b) and one case shown in Fig. 4d. (d, e) Phase diagrams summarizing types of clusters emerging under various conditions of $k_{t,A}$ and R_{ACP} for (d) $<L_f>$ = 1 μm and (e) $<L_f>$ = 1.6 μm. Red circle, black cross, and cyan square represent fluctuating cluster, small pulsatile cluster, and irreversible/decaying cluster, respectively.

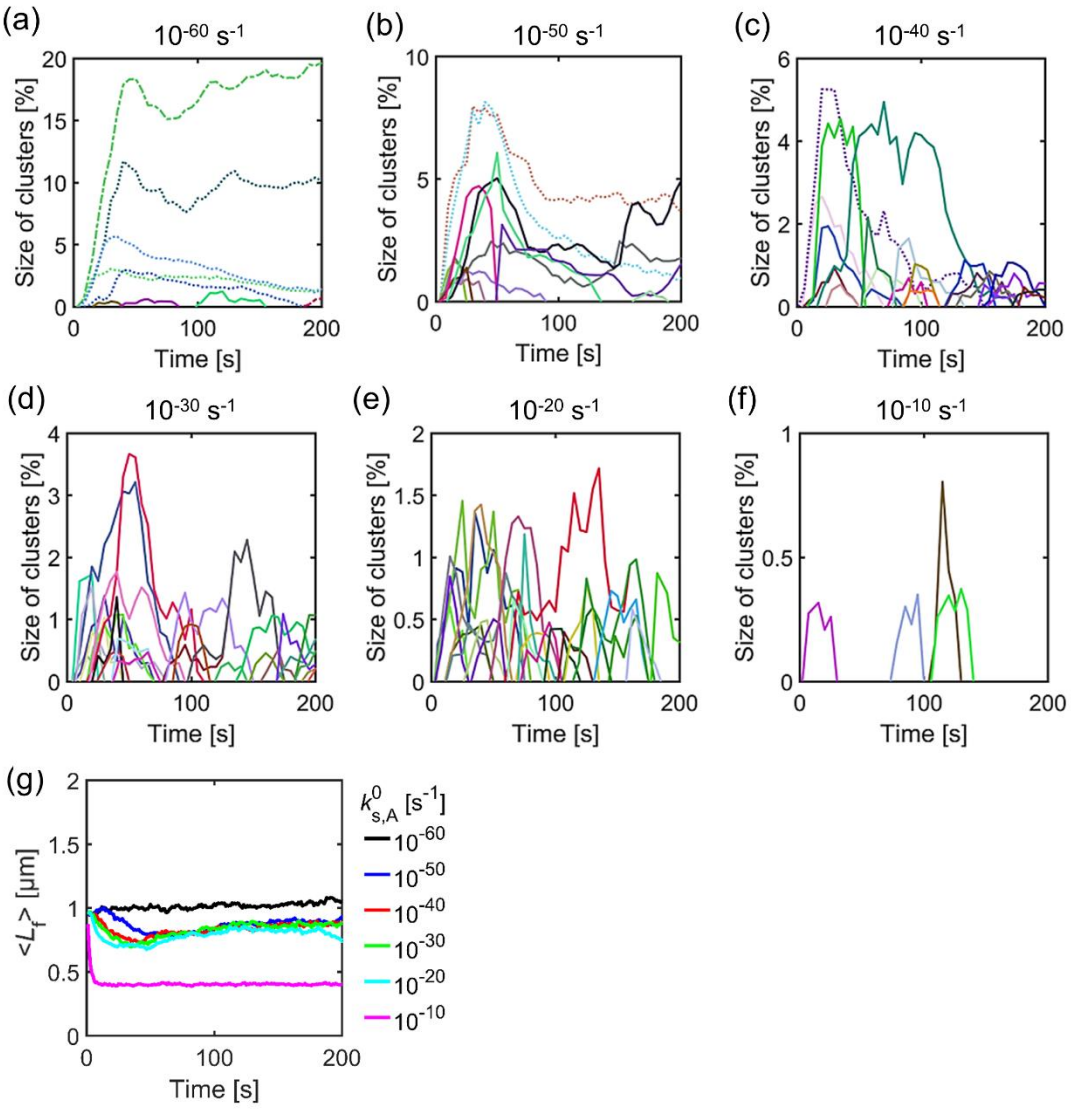

Figure S4. Effects of the zero-angle severing rate constant ($k^0_{s,A}$). Cases shown here are the same as those shown in Fig. 5. We varied $k^0_{s,A}$ between 10^{-60} s^{-1} and 10^{-10} s^{-1} at R_M = 0.04, R_{ACP} = 0.02, and $k_{t,A}$ = 30 s^{-1}. (a-f) Time evolution of percentage of actin segments located within all identified clusters. Random colors are used for curves to distinguish each cluster. Pulsed, decaying, and irreversible (fluctuating and growing) clusters are represented by solid, dotted, and dot-dashed lines, respectively. (g) Time evolution of average length of F-actins (<L_f>) for 6 cases shown in (a-f). An increase in $k^0_{s,A}$ does not shorten F-actins much in most cases except a case with $k^0_{s,A}$ = 10^{-10} s^{-1}.

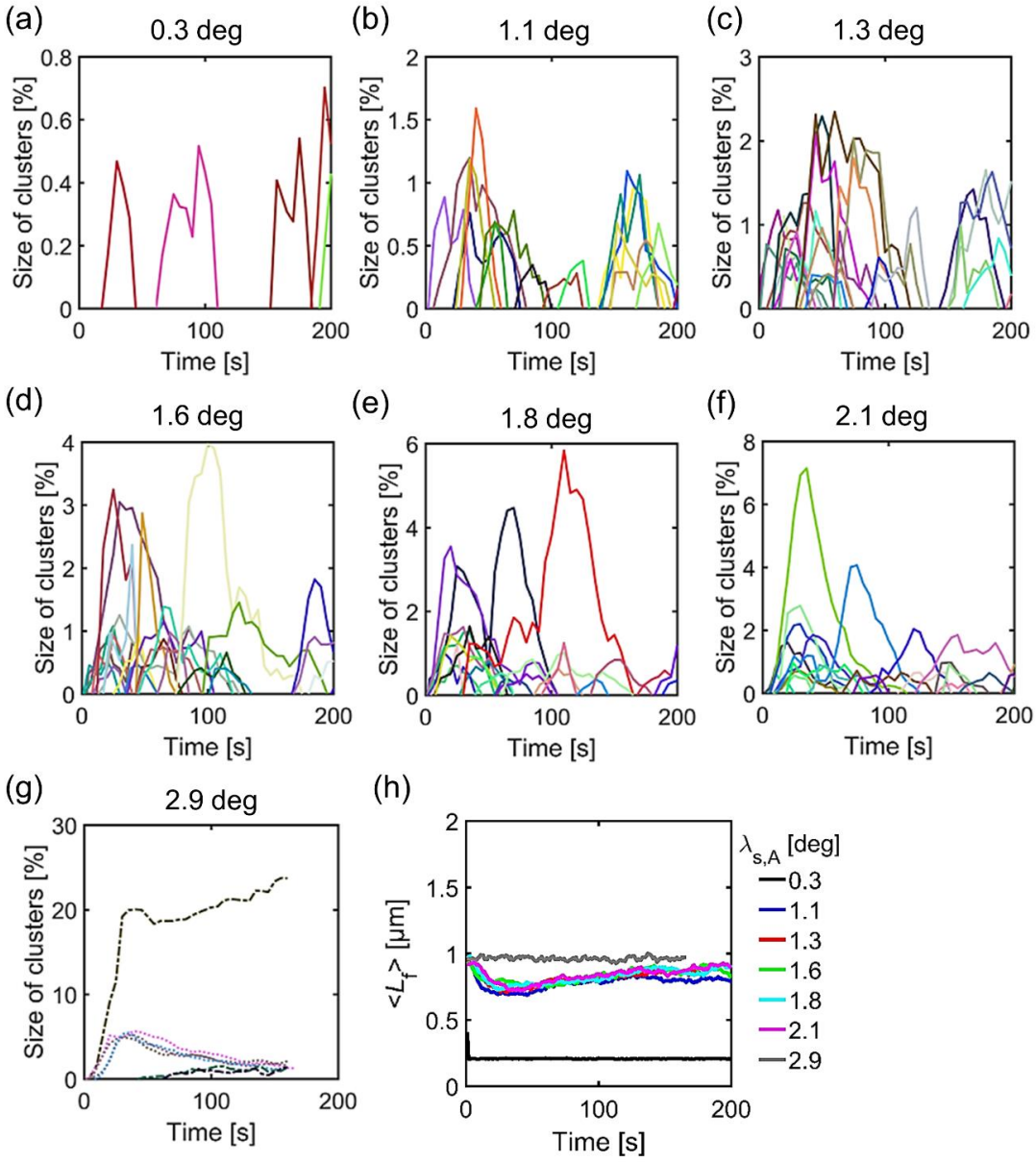

Figure S5. Impacts of insensitivity of severing to a bending angle ($\lambda_{s,A}$). Cases shown here are the same as those shown in Fig. 6. (a-g) Time evolution of percentage of actins located within all identified clusters. Random colors are assigned to curves to distinguish each cluster. Pulsed, decaying, and irreversible (fluctuating and growing) clusters are shown by solid, dotted, and dot-dashed lines, respectively. (h) Time evolution of average length of F-actins ($<L_f>$) for 7 cases shown in (a-g). A change in $\lambda_{s,A}$ does not affect $<L_f>$ significantly except in a case with $\lambda_{s,A}$ = 0.3 deg.

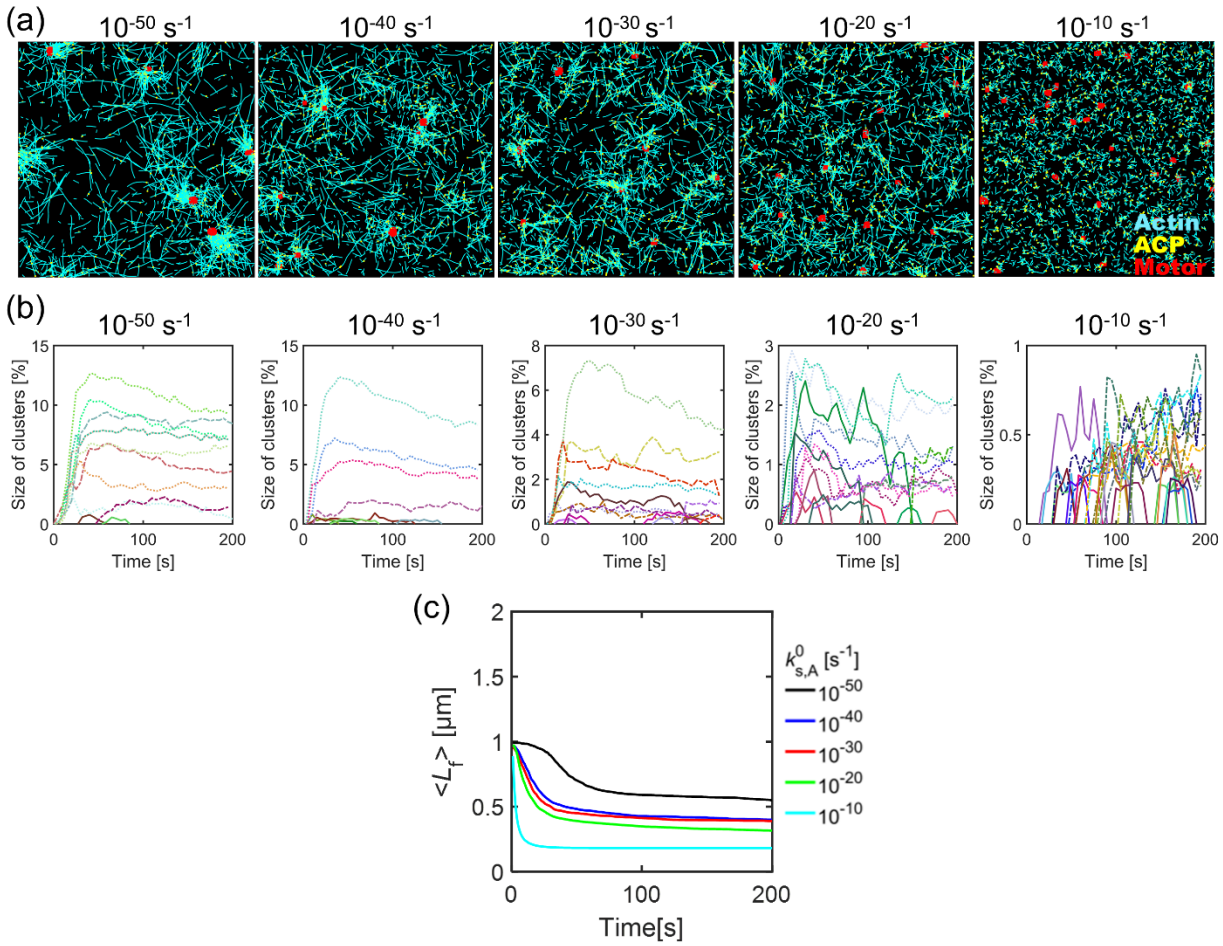

Figure S6. Simulations with various zero-angle severing rate constants ($k^0_{s,A}$) without F-actin treadmilling. We varied $k^0_{s,A}$ between 10^{-60} s^{-1} and 10^{-10} s^{-1} at R_M = 0.04, R_{ACP} = 0.02, $<L_f>$ = 1 μm, $k_{t,A}$ = 0 s^{-1}, and $\lambda_{s,A}$ = 1.6 deg. (a) Morphology of networks with various $k^0_{s,A}$. (b) Time evolution of percentage of actin segments located within clusters. Random colors are employed for curves to distinguish each cluster. Pulsed, decaying, and irreversible (fluctuating and growing) clusters are indicated by solid, dotted, and dot-dashed lines, respectively. (c) Time evolution of average length of F-actins ($<L_f>$) for 5 cases shown in (a-b). Unlike cases shown in Figs. 5 and S3, $<L_f>$ decreases more over time as $k^0_{s,A}$ is larger.

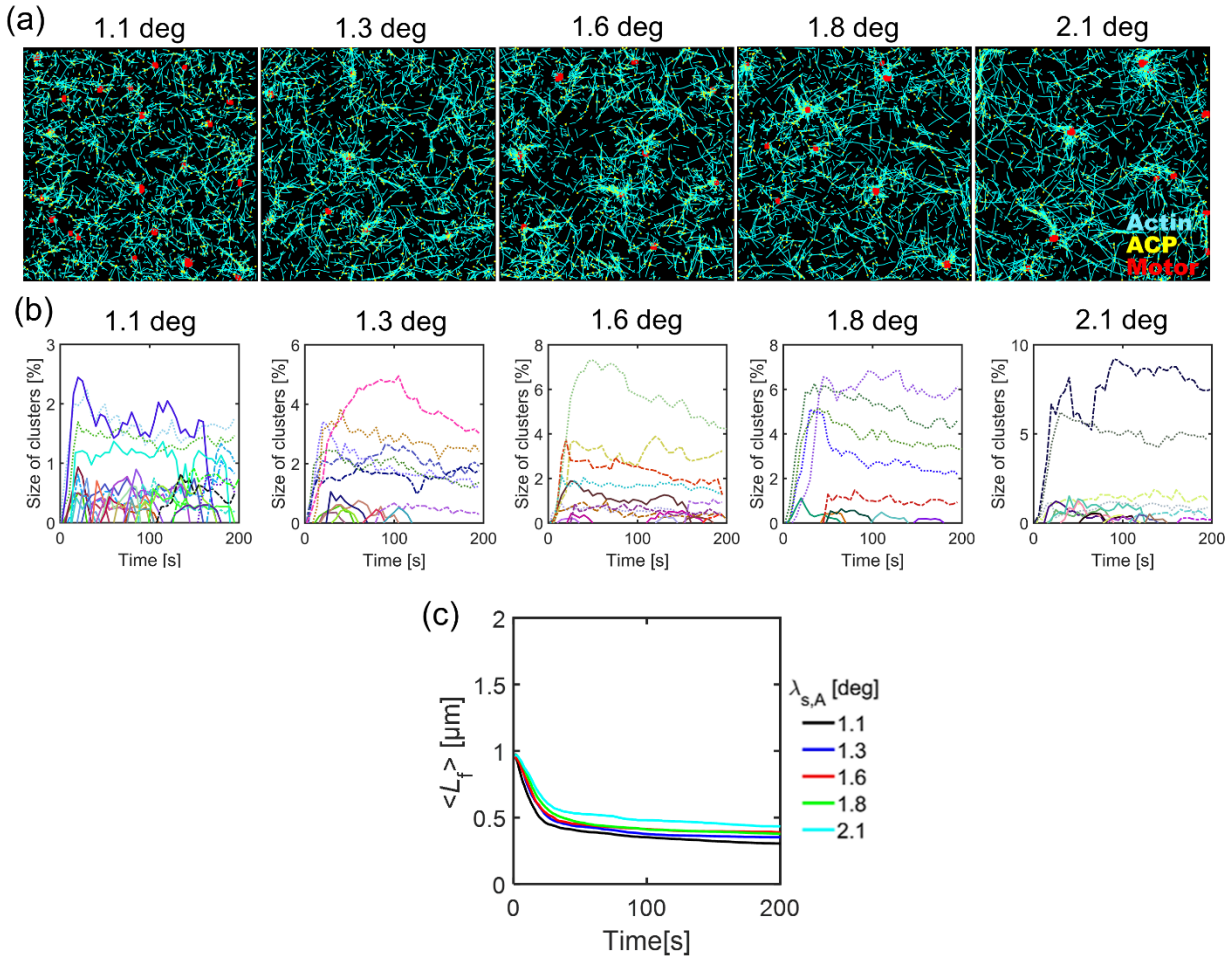

Figure S7. Simulations with different angle insensitivity of severing ($\lambda_{s,A}$) without F-actin treadmilling. We modulated $\lambda_{s,A}$ at R_M = 0.04, R_{ACP} = 0.02, $<L_f>$ = 1 μm, $k_{t,A}$ = 0 s^{-1}, and $k^0_{s,A}$ = 10^{-30} s^{-1}. (a) Morphology of networks with various $\lambda_{s,A}$. (b) Time evolution of percentage of actin segments located within clusters. Random colors are assigned to curves to distinguish each cluster. Pulsed, decaying, and irreversible (fluctuating and growing) clusters are shown by solid, dotted, and dot-dashed lines, respectively. (c) Time evolution of average length of F-actins ($<L_f>$) for 5 cases shown in (a-b). Unlike cases shown in Fig. 6, $<L_f>$ decreases significantly over time to a similar extent.

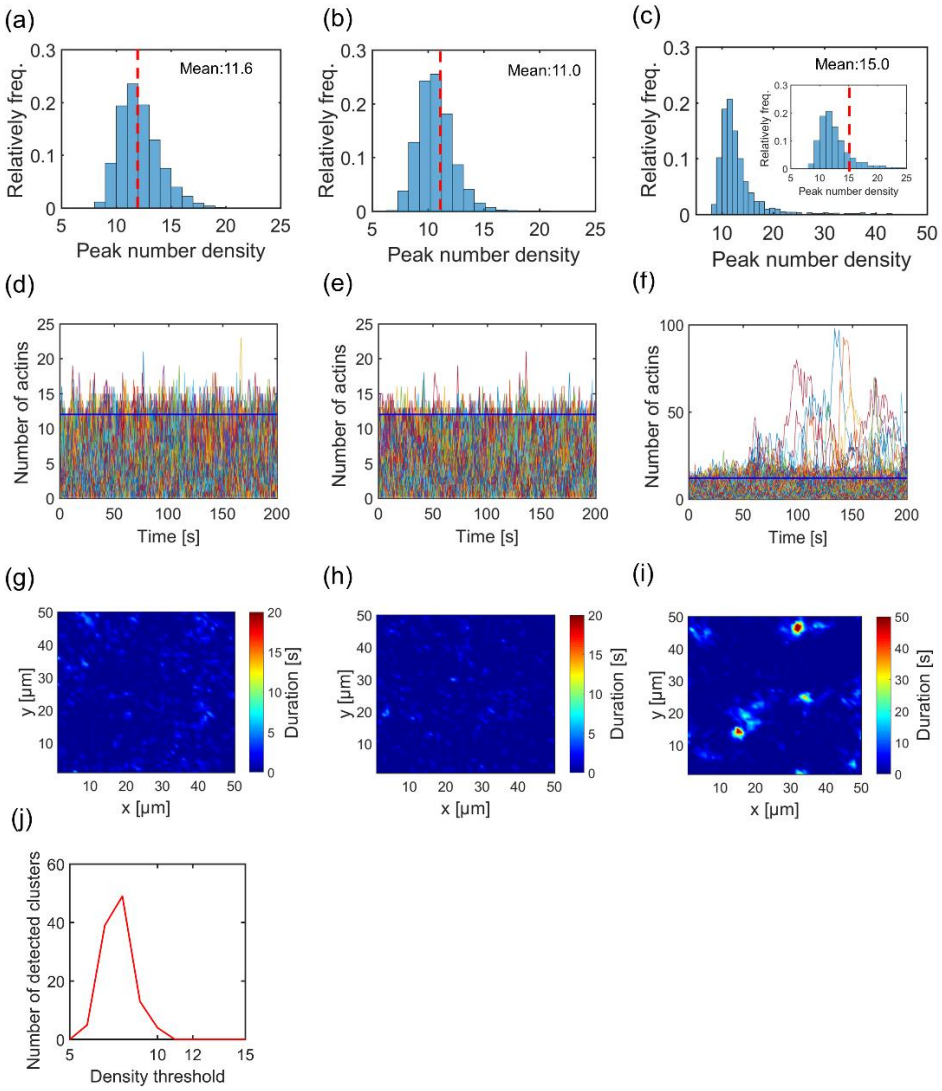

Figure S8. Justification for the threshold values used for detection of pulsed clusters. For comparison, we chose three representative cases: (a, d, g) $R_M = 0.04$, $k_{t,A} = 120\ s^{-1}$, (b, e, h) $R_M = 0$, $k_{t,A} = 60\ s^{-1}$, and (c, f, i) $R_M = 0.04$, $k_{t,A} = 70\ s^{-1}$. In all the three cases, $R_{ACP} = 0.02$, and $\langle L_f \rangle = 1.0$ μm. (a-c) Distribution of peak actin density in all grids. Dashed lines indicate mean values. Inset in (c) shows the same histogram with the same x range as that of (a) and (b) for comparison. (d-f) Time evolution of the actin density in all grids. Each curve corresponds to fluctuation in an individual grid. The blue horizontal lines indicate a chosen density threshold (~12). (g-i) Distribution of the duration of detected clusters whose density is above the density threshold. (j) The number of pulsed clusters detected in a network shown in (a, d, g), depending on the value of a density threshold. Note that the number density of actins in each cluster is divided by the total number of actins to get the size of cluster (percentage).

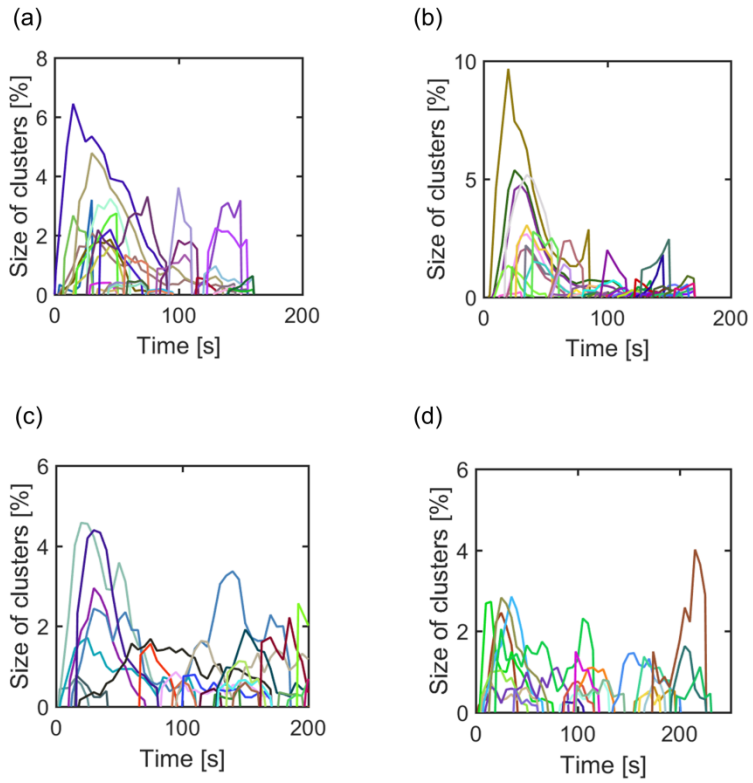

Figure S9. Pulsed contraction with different model assumptions. These plots show time evolution of percentage of actins located within all identified clusters. Random colors are assigned to curves to distinguish one cluster from the others. In (a, b), we employed shorter cylindrical segments (70 nm) for simplification of F-actin, instead of 140 nm, with (a) $\lambda_{s,A}$ = 2.2 deg, and = 10^{-20} s^{-1} and (b) $\lambda_{s,A}$ = 1.6 deg, and = 10^{-35} s^{-1}. In (c, d), it is assumed that F-actin severing occurs deterministically at a bending angle beyond (c) 160° and (d) 120°.

MOVIE CAPTIONS

Movie S1. Contractile movement of an actomyosin network showing emergence of small pulsatile clusters with $k_{t,A}$ = 80 s^{-1} (R_M = 0.04, R_{ACP} = 0.01, and $<L_f>$ = 1 μm). F-actin, ACP, and motor are visualized by cyan, yellow, and red, respectively.

Movie S2. Contractile motion of an actomyosin network with $k_{t,A}$ = 70 s^{-1} (R_M = 0.04, R_{ACP} = 0.01, and $<L_f>$ = 1 μm)**.** Fluctuating clusters are observed in addition to small pulsatile clusters. F-actin, ACP, and motor are visualized by cyan, yellow, and red, respectively.

Movie S3. Irreversible contraction of an actomyosin network with $k_{t,A}$ = 30 s^{-1} (R_M = 0.04, R_{ACP} = 0.01, and $<L_f>$ = 1 μm)**.** Several decaying clusters and growing clusters emerge. Some small clusters still appear at early times but disappear very quickly. F-actin, ACP, and motor are visualized by cyan, yellow, and red, respectively.

Movie S4. Contractile motion of an actomyosin network showing large pulsatile clusters with both F-actin turnover and severing (R_M = 0.04, R_{ACP} = 0.02, $<L_f>$ = 1 μm, $k_{t,A}$ = 30 s^{-1}, $\lambda_{s,A}$ = 2.5 deg, and $k^0_{s,A}$ = 10^{-30} s^{-1})**.** F-actin, ACP, and motor are visualized by cyan, yellow, and red, respectively.

Movie S5. Movements of an actomyosin network with F-actin severing without F-actin turnover (R_M = 0.04, R_{ACP} = 0.02, $<L_f>$ = 1 μm, $k_{t,A}$ = 0 s^{-1}, $\lambda_{s,A}$ = 1.6 deg, and $k^0_{s,A}$ =10^{-40} s^{-1})**.** F-actin, ACP, and motor are visualized by cyan, yellow, and red, respectively.

SUPPLEMENTAL REFERENCES

1. Tyska, M. J., D. E. Dupuis, W. H. Guilford, J. B. Patlak, G. S. Waller, K. M. Trybus, D. M. Warshaw, and S. Lowey. 1999. Two heads of myosin are better than one for generating force and motion. Proceedings of the National Academy of Sciences of the United States of America 96(8):4402-4407.
2. Underhill, P. T., and P. S. Doyle. 2004. On the coarse-graining of polymers into bead-spring chains. Journal of non-Newtonian fluid mechanics 122(1):3-31.
3. Clift, R., J. R. Grace, and M. E. Weber. 2005. Bubbles, drops, and particles. Courier Corporation.
4. Isambert, H., P. Venier, A. C. Maggs, A. Fattoum, R. Kassab, D. Pantaloni, and M. F. Carlier. 1995. Flexibility of actin filaments derived from thermal fluctuations. Effect of bound nucleotide, phalloidin, and muscle regulatory proteins. The Journal of biological chemistry 270(19):11437-11444.
5. Kim, T., W. Hwang, H. Lee, and R. D. Kamm. 2009. Computational analysis of viscoelastic properties of crosslinked actin networks. PLoS computational biology 5(7):e1000439.
6. Jung, W., M. P Murrell, and T. Kim. 2015. F-actin cross-linking enhances the stability of force generation in disordered actomyosin networks. Computational particle mechanics 2(4):317-327.
7. Bell, G. I. 1978. Models for the specific adhesion of cells to cells. Science 200(4342):618-627.
8. Ferrer, J. M., H. Lee, J. Chen, B. Pelz, F. Nakamura, R. D. Kamm, and M. J. Lang. 2008. Measuring molecular rupture forces between single actin filaments and actin-binding proteins. Proceedings of the National Academy of Sciences of the United States of America 105(27):9221-9226.
9. Erdmann, T., P. J. Albert, and U. S. Schwarz. 2013. Stochastic dynamics of small ensembles of non-processive molecular motors: the parallel cluster model. The Journal of chemical physics 139(17):175104.
10. Erdmann, T., and U. S. Schwarz. 2012. Stochastic force generation by small ensembles of myosin II motors. Physical review letters 108(18):188101.

11. Kim, T. 2015. Determinants of contractile forces generated in disorganized actomyosin bundles. Biomechanics and modeling in mechanobiology 14(2):345-355.
12. Jung, W., M. P. Murrell, and T. Kim. 2016. F-Actin Fragmentation Induces Distinct Mechanisms of Stress Relaxation in the Actin Cytoskeleton. Acs Macro Lett 5(6):641-645.
13. McCullough, B. R., E. E. Grintsevich, C. K. Chen, H. Kang, A. L. Hutchison, A. Henn, W. Cao, C. Suarez, J. L. Martiel, L. Blanchoin, E. Reisler, and E. M. De La Cruz. 2011. Cofilin-linked changes in actin filament flexibility promote severing. Biophysical journal 101(1):151-159.
14. Wioland, H., A. Jegou, and G. Romet-Lemonne. 2018. Torsional stress generated by ADF/cofilin on cross-linked actin filaments boosts their severing. bioRXiv.
15. Kishino, A., and T. Yanagida. 1988. Force measurements by micromanipulation of a single actin filament by glass needles. Nature 334(6177):74-76.
16. Meyer, R. K., and U. Aebi. 1990. Bundling of actin filaments by alpha-actinin depends on its molecular length. The Journal of cell biology 110(6):2013-2024.